Spatial confinement of atomic excitation by composite pulses in a doped solid

Markus Stabel ,[1,*] Niels Joseph ,[1] Nikolay V. Vitanov ,[2] and Thomas Halfmann [1,†]
[1] *Institute for Applied Physics, Technical University of Darmstadt, Hochschulstr. 6, 64289 Darmstadt, Germany*
[2] *Center for Quantum Technologies, Department of Physics,*
Saint Kliment Ohridski University of Sofia, 5 James Bourchier Boulevard, 1164 Sofia, Bulgaria

(Received 26 April 2024; accepted 23 July 2024; published 26 August 2024)

We experimentally demonstrate spatial confinement of atomic excitation by narrow-band composite pulse (NCP) sequences in a rare-earth ion-doped Pr^{3+}:Y_2SiO_5 crystal. The experimental data confirm that NCP sequences localize excitation far below the diameter of the driving laser pulse, with potential to proceed below the diffraction limit. We reach significant improvement of the spatial confinement compared to previous implementations. To this end, we derive several new classes of composite pulses that significantly outperform previously known sequences for the objectives of this study. In particular, the new NCP sequences are applicable also in inhomogeneously broadened ensembles, where most conventional composite pulse sequences fail. We systematically investigate the performance of the different classes of sequences and compare the results with numerical simulations, which agree very well with our experimental data. The findings serve as a step towards novel applications of composite pulse sequences to precisely prepare and manipulate excitation patterns in space, e.g., in quantum technology to address qubits with large spatial resolution.

DOI: 10.1103/PhysRevA.110.023526

I. INTRODUCTION

The spatial resolution of optical interactions is typically limited by the diameter of the driving laser beams in the interaction region, which in turn is limited by diffraction to about half the wavelength. Overcoming this diffraction limit is of relevance for a large range of applications, e.g., in high-resolution microscopy [1–6], nanolithography [7–11], or quantum technology, where confined atomic excitation enables, e.g., single-site addressing of tightly spaced qubits in an ion trap or optical lattice to increase the qubit interaction for quantum computations [12–17], selective addressing of single emitters from a large ensemble as isolated qubits [18–20], increasing the storage capacity of a quantum memory [21,22], the generation of narrow waveguide-like excitation structures in crystals to enhance light-matter interaction for quantum information processing [23], or patterning of Bose-Einstein condensates [11,24]. Finally, also investigations of fundamental quantum physics, e.g., the measurement of the wave function of individual or ensembles of atoms, at resolutions below the diffraction limit become possible [25–28].

This large potential for applications led to the development of a variety of approaches to overcome the diffraction limit. The best known is probably stimulated emission depletion (STED) microscopy [2]. However, STED (and related techniques) rely purely on incoherent interactions. This is an obstacle for applications which require maintenance of coherence as, e.g., in quantum information technology. Thus, in the recent three decades techniques based on coherent light-matter interactions were considered for "subwavelength localization." Early examples of these schemes made use of spatially varying potentials, but most proposals and implementations utilize spatially selective interaction with two or more laser fields (see [29] and references therein, or recent work on localization by stimulated Raman adiabatic passage [11,22] and references therein).

Recently, also composite pulse (CP) sequences were investigated to overcome the diffraction limit. CP sequences [30–32] are well known in NMR spectroscopy [30,31] and applied optics [33,34], but in the last decade also attracted attention for quantum information processing [32,35,36]. CPs are a series of pulses with their phases as control parameters, which drive a two-level quantum system on specific pathways through Hilbert space, such that the excitation probability is very robust with regard to fluctuations of experimental parameters (which is the aim of a broad-band CPs), or such that excitation occurs only for very specific experimental parameters (which is the aim of narrow-band CPs). Thus, the latter narrow-band CP (NCP) sequences show a strong dependence on experimental parameters, e.g., the driving laser intensity. This steep nonlinear dependence of the coherent excitation probability upon the intensity allows for spatially highly localized excitation, tightly confined in the center of a spatial laser beam profile, far below the beam diameter and even below the diffraction limit. We note that CPs can be considered as a special and experimentally rather easy to implement case of optimal control theory (for an overview of such techniques, see, e.g., [37,38]), with the phases of identical pulses in a sequence as discrete control parameters. In principle, it should be also possible to investigate the potential of other optimal control strategies to overcome the diffraction limit.

*Contact author: markus.stabel@physik.tu-darmstadt.de
†http://www.iap.tu-darmstadt.de/nlq

In comparison to previous techniques for coherent subwavelength localization, NCP sequences feature a number of important advantages: They do not require the qubit to be in a specific initial state [30,39,40] and use only a single optical transition (driven by a single laser beam) in a two-level system. This makes them easier to implement experimentally. If the aim is excitation of metastable states via multilevel schemes, NCPs can be extended to such systems as well [41–43]. Moreover, beyond spatial confinement of atomic excitations, NCPs also permit implementation of arbitrary narrow-band qubit rotations, i.e., localized single-qubit [17,39,44] and multiqubit gates [45].

Literature contains a wide variety of NCP sequences [15,16,39,46–49] which were initially meant to, e.g., increase the resolution in NMR spectroscopy [47,48,50]. In previous theory work [15] we suggested their application also for high-resolution addressing of qubits. In a first experimental demonstration, Merrill *et al.* implemented NCPs to reduce the ion spacing of a surface trap by about 40% [17]. Since then, we developed other classes of NCP sequences, which promise better confinement [46]. However, there were so far no experimental implementations of these sequences, in particular, not in solid-state systems nor media with inhomogeneous broadenings.

In this paper, we present a thorough, systematic experimental study of several classes of NCP sequences, applied to localize atomic excitation in a rare-earth ion-doped crystal. We develop and implement new classes of sequences, one of which is optimized specifically for inhomogeneously broadened media. We experimentally compare the performance of all new sequences, also to previously known sequences [15,16,39,46–49], as well as numerical simulations. The proof-of-principle experiment still operates above the diffraction limit, but fully confirms the theoretical predictions, thus paving the way for further investigations towards high-resolution applications.

II. BASIC THEORY

We now briefly review the basic theory of NCP sequences and introduce the new sequences, which we developed for the experiments presented below. We assume a two-level system with population initially in the ground state $|1\rangle$ resonantly coupled to the excited state $|2\rangle$ by a laser beam with Rabi frequency $\Omega(t)$ [see Fig. 1(a)]. We get the excitation probability to state $|2\rangle$ as $P_2 = \sin^2(A/2)$, with the pulse area $A = \int \Omega(t)\mathrm{d}t$. For pulsed excitation with peak Rabi frequency Ω_0 and duration τ we have $A \propto \Omega_0\tau$. As a simple and well-known example, the excitation probability reaches 100%, if the pulse area equals π. This defines the well-known π pulse, which inverts the quantum system.

Obviously, the excitation probability depends upon the experimental parameters, e.g., spatiotemporal variations or fluctuations of the Rabi frequency (which depends upon the laser intensity). Let us call this variation of $P_2(x)$ upon a specific experimental parameter x (e.g., laser frequency, intensity, pulse area, or position across the laser beam profile) an "excitation profile." We can modify the shape of the excitation profile by replacing the single driving pulse with a sequence of pulses with different phases. The phases act as control parameters that allow us to shape the profile. This is the general concept of CP sequences [30–32]. We note that it would also be possible to use other pulse parameters like the detuning or pulse area as control parameters [30,31,51–53]. Depending on the application, we can derive CP sequences for any desired manipulation of a two-level quantum system, i.e., any target rotation of the state vector on the Bloch sphere. We can either derive sequences which are more robust or more susceptible to variations of the experimental parameters compared to a single driving pulse. This results either in broad-band or narrow-band CP sequences.

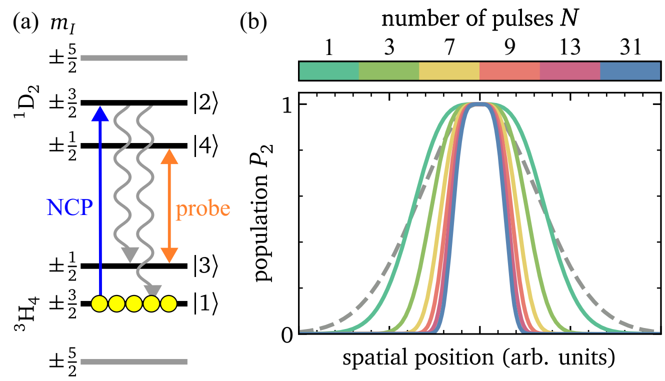

FIG. 1. (a) Coupling scheme for the NCP experiments in Pr^{3+}:Y_2SiO_5. Straight lines depict transitions coupled by a laser, wavy lines show spontaneous decay. Yellow circles show the initial population. (b) Numerical simulation of the excitation probability by NCP sequences from [16] as an example. The plot shows the variation of the final population P_2 vs spatial position across a Gaussian pump laser profile for different numbers of pulses N (color code). The gray, dashed line shows the Gaussian profile of the pump laser Rabi frequency. The pulse area in the center of the beam is set to $A = \pi$.

In this work, we focus our attention on sequences that show narrow-band behavior regarding the pulse area when it changes from its target value π, e.g., to provide excitation probability 100% in the center of a laser beam profile. The NCP sequences shall suppress excitation for $A \neq \pi$ outside the center of the laser beam profile. In the NCP we assume now a sequence of π pulses with different phases as control parameters. The pulse frequencies are all tuned exactly on resonance of the transition between ground and excited state and, hence, the detuning $\Delta = 0$. We denote such a NCP sequence consisting of N pulses with phases ϕ_k as $(\phi_1, \phi_2, \ldots, \phi_N)$.

We depict the effect of NCPs upon the spatial distribution of atomic excitation across a driving laser profile in Fig. 1(b). The figure plots the simulated population transfer in a two-level system, driven by NCP sequences with varying number of pulses N (with phases of the specific sequences as derived in previous work [16]) across a Gaussian laser beam profile in space with $A = \pi$ in the center. For a single pulse, the excitation profile has the same width [full width at half-maximum (FWHM)] as the exciting beam (compare turquoise and gray, dashed lines) since for half of the peak Rabi frequency, i.e., $A = \pi/2$, we get $P_2 = \frac{1}{2}$ from the resonance formula. Note that we consider here the Rabi frequency profile, not the intensity profile. When we replace the single pulse by a sequence with $N = 3$ pulses at appropriate phases, the NCP sequence suppresses excitation in the wings of the beam profile (where $A < \pi$) while the transfer probability in the center (where $A = \pi$) remains at 100%. Increasing the number of pulses in the NCP sequence (and choosing appropriate phases) further improves the spatial confinement of atomic excitation. This is due to the increasing number of control parameters (phases of N pulses) that are available to optimize the sequence, i.e., reduce residual deviations from full suppression of excitation outside the center.

After an early analytical theory approach in [16], further work derived NCPs with improved performance [46] by numerical procedures, though only for up to $N = 11$ pulses, while further improvements are expected for more pulses. Therefore, we extended this approach now to more pulses and derived a new class of NCPs. We chose an antisymmetric structure, i.e., sequences of the form $(\phi_1, \phi_2, \ldots, \phi_l, \phi_{l+1} = 0, -\phi_l, \ldots, -\phi_2, -\phi_1)$ with $N = 2l + 1$, based on numerical hints and to shorten the calculation. The basic theory approach was to calculate the propagator of the sequence to determine the excitation probability $P_2(A)$ versus the pulse area A (which is proportional to the Rabi frequency). Then we used numerical optimization to reduce P_2 below a certain excitation threshold ϵ in as broad intervals on both sides of the central peak (at $A = \pi$) as possible. For details on the derivation, see Appendix A. The larger the threshold ϵ, the stronger the spatial confinement of excitation close to the central peak, i.e., the narrower the excitation profile. We derive these antisymmetric sequences for up to $N = 45$ pulses with $\epsilon = 1\%$, 3%, and 10%. Tables II–IV in Appendix C give the phases of these sequences.

During systematic numerical studies we found that many previously published NCP sequences and also our new antisymmetric NCPs yield large excitation probabilities close to unity for off-resonant excitation at rather small pulse areas. This is irrelevant in the case of resonant excitation, as discussed above. However, it becomes an obstacle for inhomogeneously broadened media. In this case, there are off-resonantly driven ensembles, which would be efficiently excited also in the lower-intensity wings of the laser profile. This counteracts the desired spatial confinement to the center of the profile. We illustrate this behavior in Fig. 2(a), where we plot the simulated transition probability of our antisymmetric $N = 13$ pulse sequence with $\epsilon = 1\%$ vs the pulse area $A \propto \Omega\tau$ and the product of detuning and pulse duration $\Delta\tau$. If we consider resonant excitation $\Delta\tau = 0$ [see solid, white line in Fig. 2(a)], we get the desired behavior of the NCP: For $A = \pi$, the transfer is complete ($P_2 = 1$), while for pulse areas $A < 0.85\pi$ population transfer is almost fully suppressed. However, for off-resonant excitation $\Delta\tau \neq 0$ (left and right of the solid, white line) the variation of the transfer probability with pulse area is rather complex, with several regions of high population transfer even at small pulse areas. This is due to an additional phase accumulated by off-resonant excitation that disturbs the required fixed-phase relation within the NCP sequence.

When we now consider an inhomogeneously broadened medium, we have a manifold of frequency ensembles. Thus, in Fig. 2(a) we must average horizontally over this distribution of detunings. The dashed lines in Fig. 2(a) indicate an inhomogeneous linewidth of 100 kHz (FWHM), as it is typical in our experiments discussed below. The dotted lines indicate an interval of twice the linewidth, which we

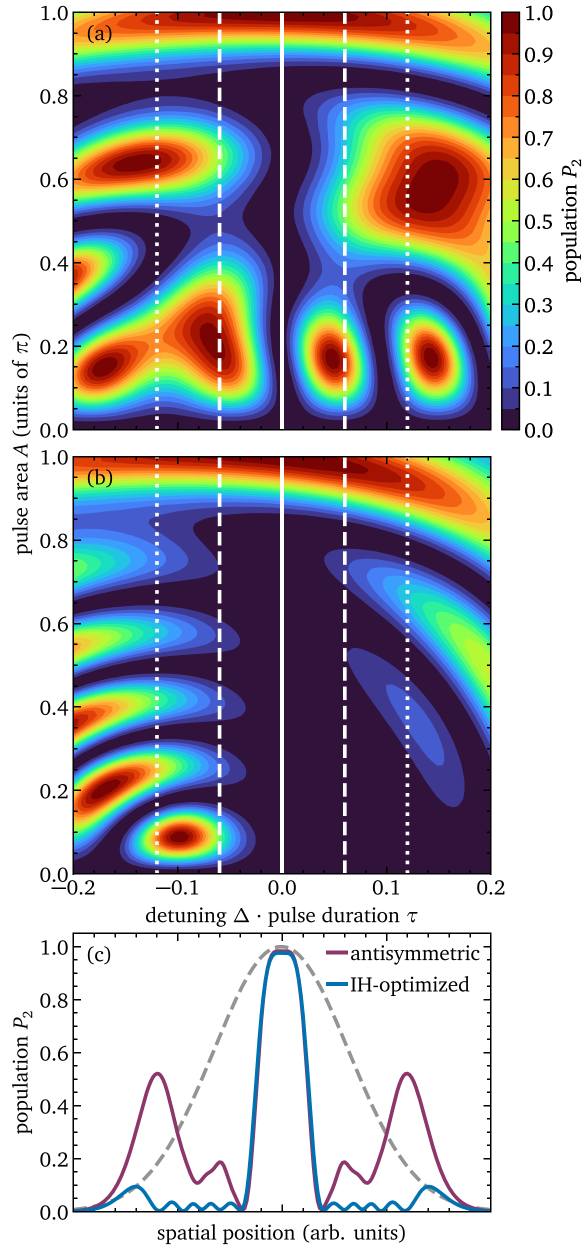

FIG. 2. Numerical simulation of the excitation probability vs the product of detuning and pulse duration $\Delta\tau$ and the pulse area A for an antisymmetric (a) and an IH-optimized (b) sequence with $N = 13$ pulses. The peak Rabi frequency is $\Omega_0 = 2\pi \times 1$ MHz. The white, dashed lines indicate the spectral linewidth of $2\pi \times 100$ kHz (FWHM) for inhomogeneous broadening in our system. The dotted lines indicate a spectral region of twice that width. (c) Variation of the final population P_2 vs spatial position across a Gaussian pump laser profile (gray, dashed line) for both NCP sequences depicted in (a) and (b). The pulse area in the center of the beam is set to $A = \pi$. All parameters are the same as in (a) and (b) and we consider the inhomogeneously broadened transition, i.e., for each spatial position and pulse area, we average the excitation probability using a Gaussian distribution of detunings matching the inhomogeneous broadening in our system [see white, dashed lines in (a) and (b)].

typically apply as limits for numerical averaging. Obviously, the detuning interval contains ensembles which experience large population transfer. Hence, as shown in Fig. 2(c), averaging leads to pronounced excitation "side bands" (an additional ringlike excitation pattern across the 2D laser beam) far in the wings of the laser beam profile at rather small pulse areas (i.e., low intensity).

We may reduce the perturbing effect of inhomogeneous broadening by using shorter pulses, which reduces the total phase accumulation. In Fig. 2, a shorter pulse duration τ essentially stretches the horizontal axis outward, moving the regions of large population transfer further from resonance. The shorter the pulses, the further the additional regions of large population transfer move from resonance, and thus a smaller fraction of these regions contributes to the averaged transfer probability. Consequently, the amplitude of the excitation side bands (rings) is reduced.

However, application of shorter pulses means increasing the Rabi frequency to maintain a π pulse in the center of the beam profile. As intensity (and Rabi frequency) are limited in the experiment, there are always limits to the minimal pulse duration. Moreover, shorter pulses also mean larger bandwidth, which may lead to unwanted couplings to additional states in the vicinity.

To overcome the problem, we developed another class of NCP sequences optimized for inhomogeneously broadened media (in the following termed "IH-optimized"). Towards this goal, we extended the numerical optimization procedure applied for the above antisymmetric NCP sequences by an additional constraint, which demands that the excitation probability is reduced below $\epsilon = 1\%$ for all detunings within a given inhomogeneous manifold. Figure 2(b) shows the excitation probability for such an IH-optimized sequence with $N = 13$ pulses. We clearly see that the regions of large excitation are shifted further from resonance than in Fig. 2(a). As such, excitation in the wings of the beam profile is suppressed [see Fig. 2(c)]. Table V in Appendix C gives the phases of the IH-optimized sequences for up to $N = 31$ pulses.

III. EXPERIMENTAL SETUP

We implement our experiments in the rare-earth ion-doped crystal Pr^{3+}:Y_2SiO_5 (from now on simply termed Pr:YSO) among the hyperfine states of the $^3H_4 \leftrightarrow {}^1D_2$ transition at a center wavelength of 605.98 nm. In particular, we choose the hyperfine states $|1\rangle = {}^3H_4\,|m_I = \pm\frac{3}{2}\rangle$ and $|2\rangle = {}^1D_2\,|m_I = \pm\frac{3}{2}\rangle$ as a two-level quantum system, driven by NCP sequences on a pump beam [see Fig. 1(a)]. The coherence time of the optical transition $T_2^e = 111$ μs sets an upper limit for the total duration of the NCP sequences or the maximal number of pulses N therein.

Figure 3(a) shows our experimental setup centered around the Pr:YSO crystal (10 mm long, 0.05% dopant concentration) which we cool to temperatures below 4 K in a continuous flow cryostat (ST-100, Janis Research Co.). We derive all laser beams in the experiment from an amplified diode laser system with frequency doubling unit (DLC PR STORAGE, Toptica Photonics). The system yields 800 mW of optical power at the experiment and is frequency stabilized to well below 100 kHz (FWHM). We apply beam lines with acousto-optical

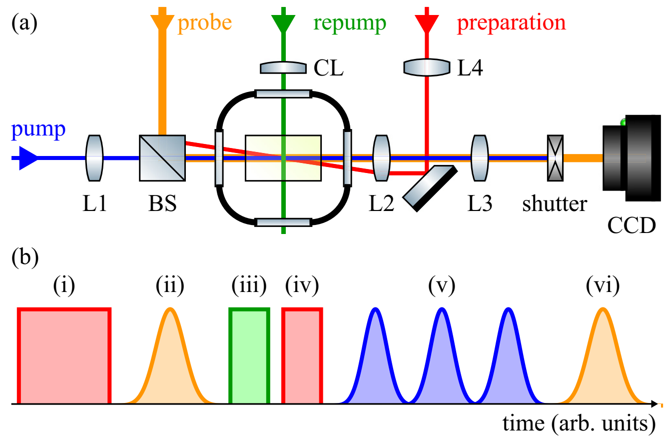

FIG. 3. (a) Experimental setup with pump (blue), preparation (red), repump (green), and probe (orange) beam lines, Pr:YSO crystal (green), beam splitter (BS), lenses (L), cylindrical lens (CL), and CCD camera. (b) Time sequence of optical pulses in the experimental sequence (see main text for details). Colors correspond to the beam lines in (a).

modulators to provide preparation, repump, pump, and probe laser pulses for the experiment with control of intensity, frequency, and phase. We employ direct digital synthesis drivers to generate the pulse shapes for preparation, repump, and probe beam, as well as an arbitrary waveform generator (AWG5014, Tektronix) for the NCP sequences on the pump beam. The latter setup permits a phase accuracy better than $\pi/200$, while NCP sequences with a few 10 pulses require an accuracy of only about $\pi/100$ (as determined by numerical simulations). The pump beam passes a spatial filter [not shown in Fig. 3(a)] to ensure a clean Gaussian beam profile before we mildly focus it into the crystal with lens L1 (focal length 200 mm), yielding a beam diameter of 210 μm (FWHM).

After the NCP sequence, the localized population in state $|2\rangle$ decays with the lifetime $T_1^e = 164$ μs mostly into states $|1\rangle$ and $|3\rangle = {}^3H_4\,|m_I = \pm\frac{1}{2}\rangle$. We note that it would be easily possible to provide very long-lived excitation patterns in Pr:YSO by mapping the excited-state population with an additional optical π pulse to a hyperfine state in the lower state $^3H_4$, which exhibits long population lifetimes $T_1^g \approx 100$ s. For our present demonstration of localization by NCP sequences we did not apply this option. Nevertheless, assuming that decay during the NCP sequence is negligible, the population distribution in state $|3\rangle$ after the decay is proportional to the population initially localized in $|2\rangle$. Hence, to determine the spatially varying population distribution after the NCP sequence, we measure the transmission across a probe laser beam profile resonant to the $|3\rangle \leftrightarrow |4\rangle = {}^1D_2\,|m_I = \pm\frac{1}{2}\rangle$ transition and compare it to a reference measurement from a fully transparent crystal. The probe beam copropagates with the pump beam, but is temporally well separated from the NCPs by roughly 7 ms. This delay is much longer than the lifetime of the excited state $T_1^e = 164$ μs, such that the population localized in state $|2\rangle$ has fully decayed when we probe it. The probe beam has a diameter of 550 μm (FWHM) in the crystal, i.e., much larger than the pump profile, to cover the full interaction region. We image the probe beam profile onto a CCD camera (Prosilica GC1290, Allied Vision) using a simple imaging system consisting of lenses L2 (focal length 60 mm) and L3 (focal length 300 mm).

We determined the magnification and resolution of the imaging system using a USAF-1951 target mask placed instead of the crystal in the beam lines. The measured resolution of 3 μm is only slightly larger than the diffraction limit given by the numerical aperture NA ≈ 0.23 of the system. The magnification of 4.93 fits with the ratio of the focal lengths of lenses L2 and L3. A mechanical shutter [54] prevents saturation of the camera caused by the pump beam.

The optical transition in Pr:YSO is inhomogeneously broadened to several GHz, while the hyperfine splitting is only on the order of 10 MHz. Hence, a single-frequency laser couples all nine transitions between the six hyperfine states of the ${}^3H_4 \leftrightarrow {}^1D_2$ transition in Pr:YSO [see Fig. 1(a)] in ions from different frequency ensembles within the inhomogeneous line. Thus, we use an optical pumping sequence to prepare the required level scheme and population distribution. The preparation sequence starts by burning a spectral pit (i.e., a broad spectral hole of vanishing absorption) that contains both the pump and probe transitions, followed by a repump pulse to create an antihole on the pump transition with a residual inhomogeneous linewidth of approximately 100 kHz (FWHM). Finally, a cleaning pulse removes unwanted population from state $|3\rangle$ to create the desired population distribution. For more details on the preparation sequence see [55,56].

The preparation beam (used to prepare the spectral pit and for the cleaning pulse) counterpropagates the pump (and probe) beam with a small angle of about 2° in-between. We collimate this beam with lenses L4 (focal length 75 mm) and L2 to a diameter of 600 μm (FWHM), ensuring good overlap with the pump beam along the entire crystal. The repump beam, on the other hand, propagates perpendicular to the other beams [see Fig. 3(a)], and we mildly focus it with a cylindrical lens (focal length 150 mm) to a size of 440 μm $\times$ 2700 μm (FWHM, width $\times$ height) in the crystal. The perpendicular arrangement of the repump beam permits us to prepare a spectral antihole (i.e., population in state $|1\rangle$) in a thin slice of the rather long Pr:YSO crystal only, while outside this slice the medium remains fully transparent for pump and probe beams. Thus, there are no attenuation or averaging effects of the latter beams in propagation direction. Due to residual saturation during the preparation sequence, the thickness of the slice and, hence, the effective interaction length with the pump and probe beam is roughly 1 mm. If required (though not relevant here), we could further reduce this value by reducing the width of the repump beam, e.g., with a cylindrical lens of shorter focal length.

Figure 3(b) summarizes the time sequence of our experiments: (i) Preparation pulse sequence to provide full transparency at the pump and probe transitions. (ii) Transmission measurement of a probe pulse as reference. (iii) Preparation of a spectral antihole on the pump transition. (iv) Removal of population from state $|3\rangle$ with a cleaning pulse. (v) NCP sequence on the pump beam. (vi) Transmission measurement of a probe pulse to determine the spatially varying excitation efficiency. In the experiment we repeat steps (i)–(vi) 50 times and average the obtained images of the probe beam to reduce noise.

IV. EXPERIMENTAL RESULTS

We will present and discuss now our experimental results on localization of atomic excitation driven by different classes of NCP sequences in Pr:YSO. For the time sequence depicted in Fig. 3(b), we choose pump pulses with a peak Rabi frequency in space and time of $\Omega_0 = 2\pi \times 1$ MHz. For a Gaussian intensity profile in time with a duration of $\tau = 332$ ns (FWHM), this corresponds to a pulse area of $A = \pi$ in the center of the pump beam profile. We truncate the pulses to a total pulse duration of $t_P = 1.2$ μs. The truncated pulses are separated by $\Delta t = 40$ ns. Theoretically, it would be possible to arrange the pulses in the NCP sequence with zero delay. However, we found that in the experiment shorter pulse separations below $\Delta t = 40$ ns lead to phase errors, presumably due to the finite rise time in the acousto-optic modulators.

With these parameters, the total duration of a composite sequence with $N = 31$ pulses (i.e., the longest sequences we investigate) is $t_C \lesssim 40$ μs, which is still sufficiently shorter than the coherence time $T_2^e = 111$ μs of the optical transition. At the same time, the Rabi frequency is well below the hyperfine splitting of the excited states (≈4.5 MHz) so that we can neglect coupling to additional states, which would modify the population transfer process.

For systematic measurements and comparison of different NCP sequences, we keep the above pulse parameters fixed and vary only the number of pulses and their phases. For each NCP sequence, we measure the population P_3 with a probe pulse of Gaussian intensity profile in time with a duration of 10 μs (FWHM) and a peak Rabi frequency of roughly $2\pi \times 15$ kHz, which leads to only negligible variation of the population distribution. We expose the CCD camera to radiation for 40 μs, which ensures detection of the entire probe pulse.

A. Spatially confined excitations by IH-optimized NCP sequences

We consider now IH-optimized NCP sequences, which are expected from theory to provide the best performance (see Sec. II above). The top row of Fig. 4 shows the experimentally measured spatial population distribution after IH-optimized NCP sequences with different numbers of pulses $N \leqslant 11$. Note that the plots show the population P_3 in state $|3\rangle$, as measured by the probe pulse after the NCP. The bottom row shows cuts (indicated by blue lines) through the central peaks.

Already the comparison of population transfer by a single π pulse and the shortest NCP with $N = 3$ pulses clearly shows spatial confinement of excitation, i.e., the diameter of the region where quantum systems are excited shrinks significantly. Population transfer that would be expected in the wings of a simple 3π pulse is essentially fully suppressed by the NCP. The central peak of large population narrows further when we increase the number of pulses in the composite sequence. For an IH-optimized NCP with $N = 11$ pulses, the population is confined to a width of roughly 40% compared to the excitation pattern after a single pulse.

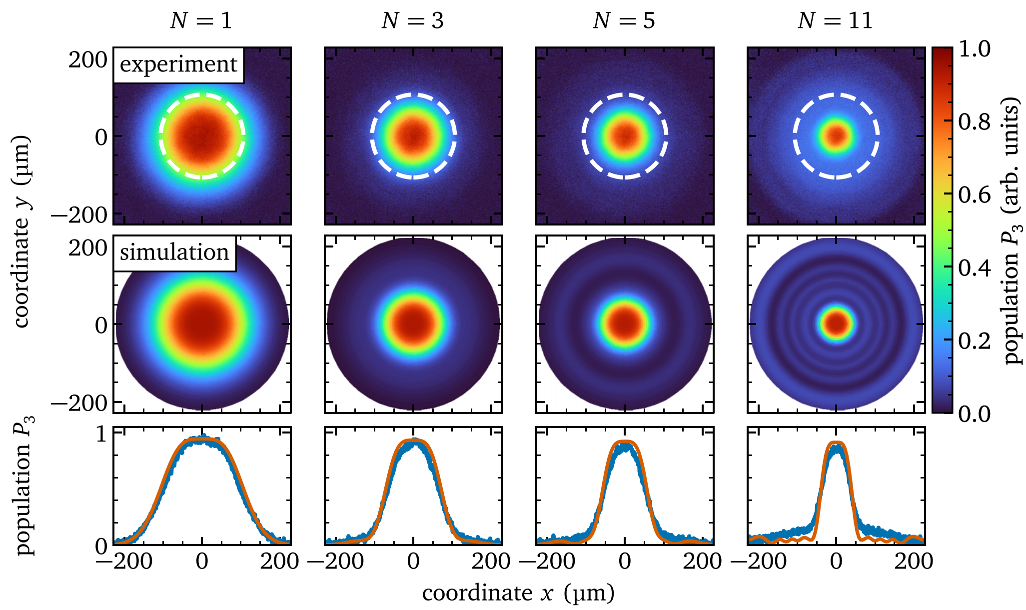

FIG. 4. NCP-driven localization in Pr:YSO using IH-optimized sequences. Variation of the population $P_3(x, y)$ vs coordinates x and y across the pump beam profile. (Upper row) Experimental data for different numbers of pulses N. The white, dashed line indicates the diameter (FWHM) of the pump beam. (Middle row) Numerical simulations. (Lower row) Cuts through the experimental data (blue line) and simulation (orange line) at coordinate $y = 0$.

We compare the results of our measurement to a straightforward numerical simulation based on a density matrix calculation of a three-level system of states $|1\rangle$, $|2\rangle$, and $|3\rangle$, coherently driven by sequences of resonant radiation pulses. The calculation takes decay of the excited state $|2\rangle$ as well as the decoherence and the inhomogeneous broadening of the optical transition $|1\rangle \leftrightarrow |2\rangle$ into account. In the calculation, we employ a Gaussian Rabi frequency distribution in space with its width matched to the experimental data, and set all other pulse parameters as in the experiment. The middle row of Fig. 4 shows the results of the simulation. The orange lines in the bottom row indicate cuts through the central peaks in the two-dimensional plots of the simulations. We see excellent agreement between experiment and simulation, with only some small deviation in the exact shape and the far wings of the excitation patterns. Compared to the simulation, the experimental data show a slightly sharper spatial confinement and a slight decrease in the peak amplitude with increasing number of pulses N. This indicates that the central pulse area in the experiment is probably slightly smaller than exactly π. From the simulation we estimate this tiny deviation to be at most 1%. We note that pass-band CP sequences [15,44,46] are insensitive to such pulse area errors and could be another option for spatially confined atomic excitations.

Furthermore, we see some faint rings in the wings of the simulated data, especially for $N = 11$. As already discussed in Sec. II, the rings are caused by inhomogeneous broadening of the optical transition [compare Figs. 2(b) and 2(c)]. However, in the experimental data, the weak rings are mostly hidden below a broad low-level background, which the simulation does not reproduce. We suspect that this residual background is due to some additional, incoherent population transfer from state $|1\rangle$ to state $|3\rangle$, e.g., by off-resonant excitation to state $|4\rangle$ or Raman scattering. In any case, neither the weak incoherent background in our particular medium and excitation scheme nor the additional rings of weak excitation in the wings of the laser profile are of any relevance to the main conclusion on the high performance of NCP sequences.

We analyze the data now in some more detail by extracting the width Δr (FWHM) of the excitation peak for IH-optimized sequences with up to $N = 31$ pulses. Figure 5 shows the (normalized) widths of the experimental data (blue circles) and the simulation (blue line) vs the number of pulses N for up to $N = 31$. Clearly, the peak width decreases with the number of pulses, as expected. We find excellent agreement up to about $N = 11$ pulses. For larger numbers of pulses, the experimentally determined profiles are slightly broader

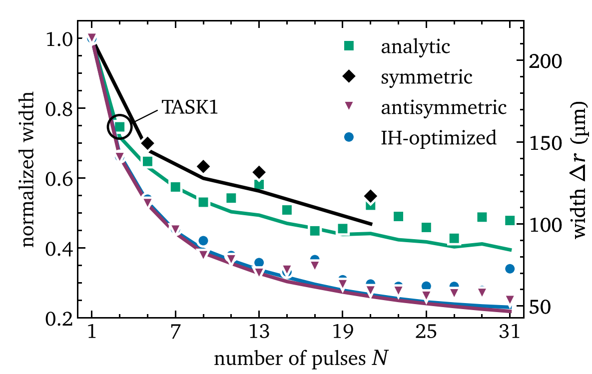

FIG. 5. Width Δr (FWHM) of the population distribution $P_3(x, y)$ after localization by four classes of NCP sequences vs number of pulses N. Comparison of experimental data (symbols) and numerical simulations (lines of the same color). The analytic sequence with $N = 3$ is equivalent to the TASK1 sequence from [17].

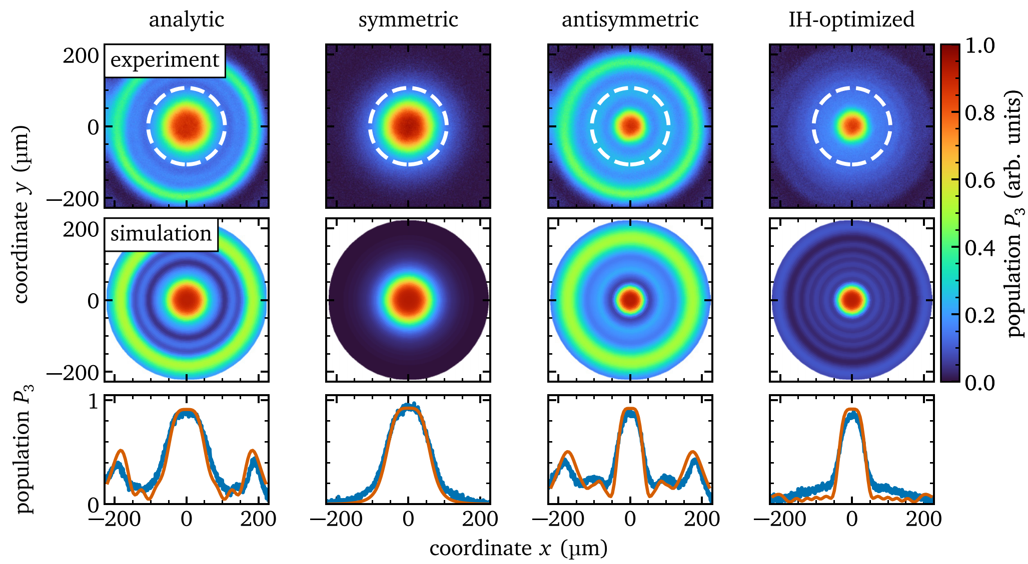

FIG. 6. NCP-driven localization in Pr:YSO using different classes of NCP sequences with $N = 13$ pulses. Variation of the population $P_3(x, y)$ vs coordinates x and y across the pump beam profile. (Upper row) Experimental data. The white, dashed line indicates the diameter (FWHM) of the pump beam. (Middle row) Numerical simulations. (Lower row) Cuts through the experimental data (blue line) and simulation (orange line) at coordinate $y = 0$.

than the simulated profiles. This is most likely caused by a small deviation of the experimental beam profile from an ideal Gaussian shape assumed in the simulation. The narrowest measured population peak with $N = 29$ pulses has a width of only about 28% of the spatial excitation pattern after a single π pulse. This again confirms the performance of NCP sequences. With our IH-optimized NCPs we reach a spatial confinement that is far below previous demonstrations with conventional sequences [17]. We note that in the latter work Merrill *et al.* characterized the improved localization with composite sequences by the separation of trapped ions at which the infidelity of a neighboring qubit reaches $\leqslant 10^{-4}$, while we use the spatial width (FWHM) of the excitation profile as a direct measure. When we apply the latter definition to their data, we find a confinement of ≈72% compared to a single pulse. In our experiment we outperform this result almost by a factor of 3.

We further analyze now the variation of the spatial confinement with the number of pulses N in the NCP sequence. To quantify this dependence, we describe the measured width Δr of the excitation by the power function

$$\Delta r(N) = N^{-\alpha} \tag{1}$$

derived in Appendix B. The larger the convergence rate α, the faster the progress towards large spatial confinement with longer NCPs. From fits to the data, we obtain exponents $\alpha = 0.38$ for the experimental data and $\alpha = 0.42$ for the numerical simulation. As discussed above, some residual deviations from ideal Gaussian-shaped π pulses lead to slightly worse performance in the experiment compared to the simulation. As also expected for NCPs, the power function shows that the gain in confinement is largest for small numbers of pulses (e.g., when we replace a single pulse by the shortest NCP sequence with three pulses), while there is slower progress for a larger number of pulses.

B. Comparison with other NCP sequences

We compare now the performance of IH-optimized NCP sequences with other classes of NCPs [15,16,39,46–49]. Except for the pulse phases of the specific sequences, all experimental parameters are the same as described in the previous section. We focus on four classes of NCP sequences, i.e., the antisymmetric and IH-optimized NCPs as derived for this work (see Sec. II above), as well as two additional classes, which we term "analytic" [16] and "symmetric" [15]. The latter are already well known from literature and are expected to exhibit the strongest suppression of excitation in the wings of a laser beam profile (under ideal conditions and without inhomogeneous broadening). Thus, we intended to compare the performance of our new sequences with the so far best alternatives. There are also some other known classes of NCP sequences, which we briefly comment on at the end of this section.

As an example for our large sets of experimental data, the top row of Fig. 6 shows the excitation profiles obtained for analytic, symmetric, antisymmetric, and IH-optimized NCP sequences with $N = 13$ pulses each. The bottom row shows cuts (indicated by blue lines) through the central peaks. Clearly, the excitation is spatially confined in all sequences, but the quality of the confinement and the excitation profiles are quite different. We find the narrowest central peak for the antisymmetric sequence, though the central peak for the IH-optimized sequence is only slightly broader. Furthermore, the analytic and antisymmetric sequences show pronounced rings around the central peak. As already discussed before, the rings are caused by inhomogeneous broadening of the optical transition (compare Fig. 2). Obviously, the IH-optimized NCP sequence combines strong confinement in a central excitation peak with a strong suppression of perturbations by inhomogeneous broadening. The numerical simulation (see middle row of Fig. 6 and orange lines in the cuts in the

TABLE I. Comparison of the convergence rate α from Eq. (1) fitted to experimental data and numerical simulations for different classes of NCP sequences.

Sequence	Excitation threshold ϵ	Convergence rate α Expt.	Convergence rate α Sim.
Symmetric [15]		0.20	0.24
Analytic [16]		0.25	0.28
IH-optimized	1%	0.38	0.42
Antisymmetric	1%	0.41	0.43
	3%	0.42	0.45
	10%	0.44	0.48

lower row) reproduces these features very well. The slightly different ring amplitudes of experimental data and simulation are most likely due to some overestimation of the inhomogeneous broadening in the simulation. Slight differences in the ring diameters suggest that the tails of the real beam profiles are a bit broader than assumed in the simulation, most likely due to an imperfect Gaussian profile in the experiment.

We performed extended systematic measurements and numerical simulations of all classes of sequences which we summarize in Fig. 5 where we show the width Δr of the central excitation peak vs the number of pulses N. In general, we see localization behavior, i.e., spatial confinement that improves with the number of pulses for all classes of sequences. As discussed, the small deviations at larger pulse numbers are most probably due to a deviation of the real laser beam profile from an exact Gaussian.

We quantify the performance of the NCP sequences for localized excitations by fitting the experimental data and the numerical simulations to the power function (1). Table I summarizes the results. For all sequences, the simulation agrees very well, with a slightly larger convergence rate α compared to the experimental data, as already discussed above. There are obvious differences between the different NCP classes with regard to their progress towards large spatial confinements, as described by the convergence rate α. In particular, the IH-optimized sequence progresses much faster to strong spatial confinements compared to the analytic and symmetric sequences. In the following we will discuss the features of the analytic, symmetric, and antisymmetric sequences in some more detail. We skip the IH-optimized sequences here, as we already discussed them in the previous section.

a. Analytic NCP sequences. We termed this class of NCP sequences analytic because previous work derived an analytic equation to determine their pulse parameters [16]. This is an advantage to quickly determine sequences with an arbitrary (odd) number of pulses. These sequences perform rather poorly compared to more recently developed NCPs. For more than $N = 5$ pulses they show pronounced rings in the excitation profile (see Fig. 6). Moreover, they progress only very slowly, with a small convergence rate $\alpha = 0.25$, towards stronger spatial confinement. This is to be expected since the analytic sequences are known to suppress excitation in the wings of the profile very well, i.e., towards less than 10^{-N} (when neglecting inhomogeneous broadening). On the other hand, the sequences with better confinement tolerate a larger level of residual excitation outside the center (given by the excitation threshold ϵ), i.e., they trade fidelity for a stronger confinement [46]. We note that the analytic NCP sequence with $N = 3$ is (up to an irrelevant global phase of $\pi/3$) equivalent to the TASK1 sequence derived by Merrill *et al.* [17]. Our experimental data fit well with this previous measurement.

b. Symmetric NCP sequences. We termed this NCP class symmetric because these sequences are symmetric with respect to reversal of pulses. They were developed in previous work [15] with a similar ansatz as the analytic sequences. Therefore, also the symmetric sequences strongly suppress excitation in the wings of the beam profile, but do not confine the excitation as well as our new antisymmetric and IH-optimized sequences. The symmetric NCPs exhibit the smallest convergence rate $\alpha = 0.2$ of the four investigated NCP classes, though still close to the value for the analytic sequences, which is also confirmed by the experimental data (see Fig. 5). We assume that the small difference compared to the analytic sequences is due to the numerical derivation rather than an exact analytic solution. As an advantage compared to the analytic sequences, the symmetric sequences show (in our experimental conditions) no rings of residual excitation in the wings of the profile (see Fig. 6). Thus, they are applicable in inhomogeneously broadened media, provided that the inhomogeneity does not become too large (about 200 kHz for our experimental parameters).

c. Antisymmetric sequences. The third class are the antisymmetric sequences developed for this work (see Sec. II). As already analyzed in detail above, in inhomogeneously broadened media these sequences show pronounced additional side bands (rings) in the excitation profile. Nevertheless, their performance to spatially confine excitation in a central peak outperforms the analytic and symmetric sequences by far, reaching a convergence rate $\alpha = 0.41$. As discussed above, this is due to the larger threshold $\epsilon = 1\%$ for residual excitation in the wings of the profile. With $N = 31$ pulses the antisymmetric sequences yield a spatial confinement of excitation to 25% of the width of the beam profile, which is slightly better than the IH-optimized sequences, reaching 28% (see Fig. 5). This is to be expected since the suppression of excitation for detuned ensembles places additional constraints on the IH-optimized sequences.

Furthermore, our data confirm that the localization of our antisymmetric sequences improves for a higher excitation threshold ϵ in the derivation (see Table I). However, this reduces the fidelity as expected. Other sequences based on a similar ansatz [46] were shown to exhibit the same behavior.

d. Other sequences. Finally, we compared our data also to several other already known NCP sequences [39,47–49]. In order not to overload the graphs, they are not shown in Figs. 5 and 6. Previous simulations [16] already demonstrated that most of these sequences perform similar or worse than the analytic sequences, with additional degradation in inhomogeneously broadened media. Our measurements confirmed these features. The sequences developed by Shaka and Freeman [47] are an exception, as they reach a spatial confinement similar to our IH-optimized sequences. However, they show excitation in the wings even under perfect conditions and their performance strongly degrades on an inhomogeneously broadened transition.

e. Summary. The above comparison of the features of different classes of NCP sequences shows that the choice depends upon the medium and specific application. When the goal is a strong confinement, the antisymmetric sequences are best suited, unless the transition is inhomogeneously broadened, which requires our IH-optimized sequences. Both sequences proceed very fast towards small excitation regions. If the aim is large fidelity (i.e., a very small level of residual excitation), the already known analytic [16] or, in case of an inhomogeneously broadened transition, symmetric sequences [15] are the best choice, though at the cost of slow convergence rates towards strong confinements.

V. CONCLUSION

We experimentally demonstrated strong spatial confinement of optical excitation in a solid-state system by novel NCP sequences. In particular we developed a pulse sequence, which maintains high performance also in inhomogeneously broadened media. We investigated NCP sequences with up to 31 pulses and confined the excitation to spatial extensions well below the diameter of the driving Gaussian laser beam profile. We reached a width of 25% compared to the diameter of the driving laser beam, which is about a factor of 3 smaller than in previous experiments [17]. We confirmed that the localization of atomic excitation improves with the number of pulses and quantified this behavior by the convergence rate in a power function. We compared the performance of several classes of NCP sequences and confirmed their very different features with regard to convergence rates and residual excitation in the wings of the laser beam profile. The extended and thorough investigations on different types of NCP sequences showed a tradeoff between strong confinement in the center of the beam profile and fidelity (i.e., low excitation level in the wings of beam profiles). We confirmed that inhomogeneous broadening leads to ringlike excitation patterns for NCP sequences, which are not matched to such media. The findings fit very well with numerical simulations and previous predictions from theory work [46].

We note that under our experimental conditions, we still operated well above the diffraction limit. Nevertheless, the NCP sequences permit to proceed also below this limit. Thus, our results serve as a step towards a new application of CPs to prepare precisely defined excitation patterns in space for high-resolution classical optics (e.g., lithography or microscopy) and quantum technology (e.g., to operate quantum gates with large spatial resolution).

ACKNOWLEDGMENTS

We thank G. Genov (Ulm University) for valuable scientific discussion. N.V.V. acknowledges partial support by the Bulgarian national plan for recovery and resilience, Contract No. BG-RRP-2.004-0008-C01 (SUMMIT), Project No. 3.1.4, and by the European Union's Horizon Europe research and innovation program under Grant Agreement No. 101046968 (BRISQ).

APPENDIX A: DERIVATION OF IH-OPTIMIZED COMPOSITE PULSES

In order to derive our new NCP sequences, we consider a two-state quantum system interacting with an external coherent field. The Schrödinger equation

$$i\hbar\partial_t \mathbf{c}(t) = \mathbf{H}(t)\mathbf{c}(t) \tag{A1}$$

describes the evolution of the qubit, where $\mathbf{c}(t) = [c_1(t), c_2(t)]^T$ is a column vector with the probability amplitudes of the two states $|\psi_1\rangle$ and $|\psi_2\rangle$. The Hamiltonian after the rotating-wave approximation is

$$\mathbf{H}(t) = (\hbar/2)\Omega(t)e^{-iD(t)}\,|\psi_1\rangle\,\langle\psi_2| + \text{H.c.}, \tag{A2}$$

with $D = \int_0^t \Delta(t')dt'$, where $\Delta = \omega_0 - \omega$ is the detuning between the field frequency ω and the Bohr transition frequency ω_0. For a constant detuning we have $D = \Delta t$. The Rabi frequency $\Omega(t)$ is a measure of the field-system interaction energy $\hbar\Omega(t)$. We describe the evolution of the quantum system by means of the propagator $\mathbf{U}(t_f, t_i)$, which connects the probability amplitudes at the initial time t_i and the final time t_f: $\mathbf{c}(t) = \mathbf{U}(t, t_i)\mathbf{c}(t_i)$. For the sake of simplicity, hereafter we drop the temporal arguments in $\mathbf{U}$.

Because the 2×2 propagator is unitary, we can parametrize it by two complex Cayley-Klein parameters a and b as

$$\mathbf{U} = \begin{bmatrix} a & b \\ -b^* & a^* \end{bmatrix}. \tag{A3}$$

For resonant excitation ($\Delta = 0$) with a pulse area A we have $a = \cos(A/2)$ and $b = -i\,\sin(A/2)$. For an off-resonant pulse of rectangular temporal shape we have

$$a = \cos\left(\frac{1}{2}\sqrt{\Delta^2 + \Omega^2}T\right) + \frac{i\Delta\,\sin\left(\frac{1}{2}\sqrt{\Delta^2+\Omega^2}T\right)}{\sqrt{\Delta^2+\Omega^2}}, \tag{A4a}$$

$$b = -\frac{i\Omega\,\sin\left(\frac{1}{2}\sqrt{\Delta^2+\Omega^2}T\right)}{\sqrt{\Delta^2+\Omega^2}}, \tag{A4b}$$

where T is the pulse duration. There are very few other temporal shapes for which (more complicated) exact expressions for a and b are known (see, e.g., Refs. [57–60]); otherwise, one has to compute a and b numerically.

A constant phase shift ϕ in the driving field $\Omega(t) \to \Omega(t)e^{i\phi}$ is mapped onto the propagator as

$$\mathbf{U}(\phi) = \begin{bmatrix} a & be^{i\phi} \\ -b^*e^{-i\phi} & a^* \end{bmatrix}. \tag{A5}$$

A sequence of N identical pulses, a CP sequence, each with a different pulse area A_k and a different phase ϕ_k ($k = 1, 2, \ldots, N$),

$$(A_1)_{\phi_1}(A_2)_{\phi_2}\ldots(A_N)_{\phi_N}, \tag{A6}$$

produces the overall propagator (acting from right to left)

$$\mathbf{U}^{(N)} = \mathbf{U}(A_N, \phi_N)\ldots\mathbf{U}(A_2, \phi_2)\mathbf{U}(A_1, \phi_1). \tag{A7}$$

The transition probability is $P_2 = |U_{21}^{(N)}|^2$. Complete population inversion means $P_2 = 1$.

If the pulse areas A_k and the phases ϕ_k are chosen appropriately one can modify the excitation profile essentially in any desired manner. In particular, one can nullify the first few terms in the Taylor expansion of the transition probability P_2 against a certain parameter at a specific value. Thereby the composite transition probability can be made much more robust to variations in this parameter in the vicinity of the chosen value than the single-pulse transition probability. CPs can be made robust to variations in essentially any desired experimental parameter as well as in several parameters simultaneously. Moreover, the transition probability can be locked to 1, or 0, or any other value in-between. In this manner one can obtain broad-band (with flat top), narrow-band (with flat bottom), and pass-band (with both flat top and flat bottom) excitation profiles.

In this paper, we are interested in *narrow-band* CPs, which produce unit transition probability at the pulse area of π, which quickly drops down to negligible values as the pulse area moves away from this value. The CPs derived by cancellation of the first few coefficients in the Taylor expansion of the transition probability at the selected parameter value (which is $A = 0$ for NCPs), e.g., the analytic [16] or symmetric [15] sequences discussed in this paper, produce excitation profiles with wings of extremely low value within a certain range of $A = 0$ [16]. Such extremely low values are not necessary in the present context. Instead, for the ultra-narrow-band pulses [46] the wings of the excitation profile are maintained below a certain low threshold ϵ. Then one can obtain CPs with broader intervals of the pulse area wherein the error remains below the selected threshold. The larger the threshold ϵ, the broader this interval can be. This results in a further squeezed (ultra-narrow-band) excitation profile compared to the standard narrow-band pulses (obtained by canceling derivatives).

The NCP sequences of Ref. [46] have been obtained by numerically maximizing the value A_ϵ, for which the transition probability remains below the threshold ϵ within the pulse area range $A \in [0, A_\epsilon]$, while keeping its unit value at $A = \pi$. Maximizing A_ϵ implies squeezing the excitation profile toward $A = \pi$ and enhancing the narrow-band effect. These sequences have been derived under the condition of exact resonance, $\Delta = 0$, while ignoring the excitation probability for $\Delta \neq 0$. We use the same ansatz with the additional constraint that the sequences be antisymmetric (see below) to derive our antisymmetric sequences with $\epsilon = 1\%$, 3%, and 10%. Tables II–IV in Appendix C give the phases of these sequences.

However, in inhomogeneously broadened ensembles of two-state atoms with transition frequencies within a certain bandwidth $[\omega - \Delta_0, \omega + \Delta_0]$ around the carrier frequency ω of the driving laser pulse, plenty of artifacts in the excitation probability may emerge within the detuning range $[-\Delta_0, \Delta_0]$ for pulse areas in the range $A \in [0, \pi]$, as shown in Fig. 2(a). Because the overall signal is an integral over this detuning range, the high-probability regions within this range generate unwanted side bands around the central peak in the experiment.

Therefore, we have developed ultra-narrow-band CPs, which clean up the high-probability artifacts within the detuning range $[-\Delta_0, \Delta_0]$ and the pulse area range $A \in [0, A_\epsilon]$. We have done this by numerically maximizing the value A_ϵ, for which the transition probability, *integrated over the detuning range* $[-\Delta_0, \Delta_0]$, remains below the value ϵ within the pulse area range $A \in [0, A_\epsilon]$. In so doing we have assumed rectangular pulse shapes.

This numerical procedure has suggested that (i) the constituent pulses should be an odd number $N = 2l + 1$, (ii) all pulse areas in the composite sequence should be equal, and (iii) the composite phases should be antisymmetric. The resulting composite sequences read as

$$A_{\phi_1} A_{\phi_2} \ldots A_{\phi_l} A_{\phi_{l+1}} A_{-\phi_l} \ldots A_{-\phi_2} A_{-\phi_1}. \tag{A8}$$

This choice ensures the transition probability $P_2 = 1$ for $A = \pi$. The transition probability is invariant to a constant phase shift in all phases and we have used this leeway to set $\phi_{l+1} = 0$. Hence, we are left with a maximization problem for A_ϵ with l free parameters, the phases from ϕ_1 to ϕ_l. For $\epsilon = 1\%$, this gives us the IH-optimized sequences discussed in the main text. We list the phases of these sequences in Table V of Appendix C. We note that these sequences are not unique. There are multiple solutions to the maximization problem yielding the same excitation probability, due to the periodic structure of the involved functions.

APPENDIX B: DERIVATION OF THE CONVERGENCE BEHAVIOR

In order to calculate the convergence behavior of NCP sequences, i.e., the relation between the localization width Δr and the number of pulses N, we start from the excitation probability to state $|2\rangle$. For an analytic sequence with N pulses it reads as [16]

$$P_2(A, N) = \sin^{2N}\left(\frac{A}{2}\right). \tag{B1}$$

Let us further assume a Gaussian Rabi frequency profile with a central pulse area of π (as in our experiments), i.e., $A(r) = \pi \exp(-r^2)$. Then, we find the width (FWHM) Δr of the resulting population peak as twice the radius r_0 at which

$$P_2(A, N, r_0) = \sin^{2N}\left(\frac{\pi}{2}\exp\left(-r_0^2\right)\right) \stackrel{!}{=} \frac{1}{2}$$

$$\Leftrightarrow \sin\left(\frac{\pi}{2}\exp\left(-r_0^2\right)\right) = \left(\frac{1}{2}\right)^{\frac{1}{2N}}. \tag{B2}$$

For $N \to \infty$, we have $(\frac{1}{2})^{\frac{1}{2N}} \to 1$ and thus $\exp(-r_0^2) \to 1$ and $r_0^2 \to 0$. Hence, we can approximate $\exp(-r_0^2) \approx 1 - r_0^2 \equiv 1 - x$ where we define $x \equiv r_0^2$. We get

$$\sin\left(\frac{\pi}{2}(1-x)\right) = \left(\frac{1}{2}\right)^{\frac{1}{2N}}$$

$$\Leftrightarrow \cos\left(\frac{\pi}{2}x\right) = \left(\frac{1}{2}\right)^{\frac{1}{2N}}. \tag{B3}$$

Since x is very small, we can approximate $\cos(\frac{\pi}{2}x) \approx 1 - \frac{\pi^2 x^2}{8}$ and get after a few algebraic transformations

$$x = \frac{2\sqrt{2}}{\pi}\sqrt{1 - \left(\frac{1}{2}\right)^{\frac{1}{2N}}}. \tag{B4}$$

We further define $y \equiv 2^{\frac{1}{2N}} - 1 \to 0$ and perform the series expansion

$$\sqrt{1 - \left(\frac{1}{2}\right)^{\frac{1}{2N}}} = \sqrt{1 - \frac{1}{1+y}} \approx \sqrt{y}. \tag{B5}$$

Thus, we get

$$r_0 = \sqrt{x} = \sqrt{\frac{2\sqrt{2}}{\pi}} y^{1/4} = \sqrt{\frac{2\sqrt{2}}{\pi}} (2^{\frac{1}{2N}} - 1)^{1/4}. \tag{B6}$$

Finally, we define $z \equiv 1/N \to 0$ and expand

$$(2^{z/2} - 1)^{1/4} \approx \left(\frac{\ln 2}{2}\right)^{1/4} z^{1/4} \tag{B7}$$

to get the end result

$$\Delta r = 2r_0 = \frac{2\sqrt{2}}{\sqrt{\pi}} (\ln 2)^{1/4} N^{-1/4}. \tag{B8}$$

The exponent in Eq. (B8) perfectly matches the convergence rate $\alpha = 0.25$ we found experimentally for the analytic sequences (compare Table I).

For all other classes of sequences, an analytic derivation of the convergence rate α is not possible since no analytic expression for the excitation probability $P_2(A, N)$ is available. However, it is reasonable to assume that the variation of the localization width follows a similar mathematical expression for all sequences. With this assumption, the exponent in Eq. (B8) is the sole parameter to define the convergence rate, i.e., how fast the width converges to strong spatial confinements. Hence, we fit our data to the power function [Eq. (1)]

$$\Delta r = N^{-\alpha}, \tag{B9}$$

where we replace the exponent $\frac{1}{4}$ with the variable convergence rate α.

APPENDIX C: PARAMETERS OF NCP SEQUENCES

The following tables (Tables II–V) list the phases of the antisymmetric and IH-optimized NCP pulse sequences, developed and demonstrated in this work. The parameters of the known analytic and symmetric sequences are available from literature [15,16].

TABLE II. Phases (in units of π) of antisymmetric sequences with excitation threshold $\epsilon = 1\%$. The sequences are antisymmetric, i.e., of the form $(\phi_1, \phi_2, \dots, \phi_l, \phi_{l+1} = 0, -\phi_l, \dots, -\phi_2, -\phi_1)$ with $N = 2l + 1$. We list only the first $l + 1$ phases.

Pulse count N	Phases $(\phi_1, \phi_2, \dots, \phi_{l+1})$
3	(0.5867, 0)
5	(0.4167, 0.6531, 0)
7	(0.4962, 0.3741, 0.6722, 0)
9	(0.2638, 0.5868, 0.9098, 0.3231, 0)
11	(1.0521, 0.8626, 0.1783, 0.286, 0.3356, 0)
13	(0.3081, 0.3103, 0.7134, 1.0449, 0.4763, 0.3045, 0)
15	(0.808, 0.7523, 0.8893, 0.5425, 1.8546, 0.0639, 1.9734, 0)
17	(0.5511, 0.5869, 0.255, 0.1629, 0.542, 0.8862, 0.4558, 0.4502, 0)
19	(0.772, 0.8166, 1.384, 1.5422, 1.6391, 1.3322, 1.6465, 0.0531, 1.8781, 0)
21	(0.7721, 0.3532, 0.3977, 0.3727, 0.2405, 0.4101, 0.8202, 0.6987, 0.6325, 0.0469, 0)
23	(0.2855, 0.5246, 0.0672, 0.2785, 0.6819, 0.9743, 0.7609, 0.7125, 0.5803, 0.2815, 1.9764, 0)
25	(0.7752, 0.7436, 0.8543, 0.9156, 0.951, 0.3405, 0.3542, 0.1142, 1.7152, 1.8812, 0.1249, 0.2441, 0)
27	(0.9106, 0.7793, 0.8741, 0.919, 0.6748, 0.1305, 0.4263, 0.3121, 0.1732, 0.031, 1.5934, 1.601, 1.8221, 0)
29	(1.592, 1.6943, 1.8226, 1.6936, 1.7099, 1.148, 1.0171, 1.2158, 1.3742, 1.1667, 1.3745, 1.755, 1.7427, 0.0888, 0)
31	(0.1506, 0.1473, 0.4329, 0.6354, 0.4592, 0.6133, 0.5471, 0.909, 0.8177, 0.8211, 0.8799, 0.2678, 0.0471, 0.1753, 0.1386, 0)
33	(0.0605, 0.3173, 0.3687, 0.3214, 0.7288, 0.691, 0.4768, 0.5922, 0.755, 1.0539, 0.9969, 0.4875, 0.5086, 0.1605, 0.0942, 1.9699, 0)
35	(0.7764, 0.8959, 0.4011, 0.3161, 0.2605, 0.1795, 0.3489, 0.6039, 0.5421, 0.2292, 0.3143, 0.6859, 0.6385, 0.7293, 0.4954, 0.4996, 0.1466, 0)
37	(1.9595, 0.0756, 0.1623, 0.3757, 0.6084, 1.002, 0.7508, 0.4055, 0.5571, 0.5575, 0.6507, 0.592, 0.8204, 0.5076, 0.553, 0.49, 0.0528, 0.0186, 0)
39	(0.1087, 0.2857, 0.1066, 0.5401, 0.5102, 0.5232, 0.6996, 0.7261, 0.3576, 0.5627, 0.9152, 1.0572, 0.921, 0.6668, 0.4357, 0.3466, 0.0842, 1.9795, 0.0811, 0)
41	(0.011, 1.9903, 0.1027, 0.1698, 0.7533, 0.6829, 0.554, 0.755, 0.6636, 0.5558, 0.3994, 0.5137, 0.7315, 0.8742, 0.634, 0.6768, 0.3095, 0.1907, 0.2657, 0.2342, 0)
43	(0.7016, 0.5836, 0.6095, 0.2795, 0.5116, 0.3351, 0.2791, 0.3566, 0.132, 0.0988, 0.6051, 0.6613, 0.5835, 0.5485, 0.7326, 0.85, 0.7427, 0.6024, 0.2946, 1.9385, 1.9916, 0)
45	(0.1309, 0.0921, 0.2904, 0.1137, 0.1668, 0.5634, 0.8871, 0.6043, 0.8313, 0.7831, 0.786, 0.7749, 0.4961, 0.4196, 0.2216, 0.3962, 0.7556, 0.6052, 0.5514, 0.4025, 0.2568, 0.0817, 0)

TABLE III. Phases (in units of π) of antisymmetric sequences with excitation threshold $\epsilon = 3\%$. The sequences are antisymmetric, i.e., of the form $(\phi_1, \phi_2, \dots, \phi_l, \phi_{l+1} = 0, -\phi_l, \dots, -\phi_2, -\phi_1)$ with $N = 2l + 1$. We list only the first $l + 1$ phases.

Pulse count N	Phases $(\phi_1, \phi_2, \dots, \phi_{l+1})$
3	(0.5478, 0)
5	(0.4014, 0.6036, 0)
7	(0.4679, 0.3661, 0.6192, 0)
9	(0.2743, 0.5479, 0.8215, 0.2737, 0)
11	(0.9405, 0.7834, 0.1544, 0.243, 0.2838, 0)
13	(0.3107, 0.3125, 0.6529, 0.9397, 0.41, 0.2559, 0)
15	(0.7374, 0.6918, 0.8046, 0.5114, 1.8791, 0.0525, 1.9782, 0)
17	(0.5133, 0.5426, 0.2648, 0.1967, 0.5245, 0.8278, 0.4145, 0.3883, 0)
19	(1.0857, 1.0493, 0.5481, 0.3897, 0.2779, 0.5719, 0.3104, 1.9541, 0.1001, 0)
21	(0.6942, 0.3357, 0.3807, 0.3709, 0.2512, 0.4053, 0.771, 0.6325, 0.5603, 0.0383, 0)
23	(0.2924, 0.4908, 0.0825, 0.316, 0.6696, 0.8921, 0.6873, 0.6276, 0.4963, 0.236, 1.9807, 0)
25	(0.7102, 0.6844, 0.7749, 0.8227, 0.8514, 0.3148, 0.3486, 0.1098, 1.7439, 1.8907, 0.1027, 0.2023, 0)
27	(0.8224, 0.7147, 0.7939, 0.8286, 0.6261, 0.1426, 0.42, 0.3223, 0.1844, 0.0327, 1.6501, 1.6654, 1.8534, 0)
29	(1.6074, 1.6911, 1.7964, 1.6895, 1.7042, 1.2068, 1.0931, 1.2621, 1.448, 1.2699, 1.4561, 1.7986, 1.7795, 0.0726, 0)
31	(0.1817, 0.1791, 0.4162, 0.5895, 0.4411, 0.5726, 0.5109, 0.8268, 0.7237, 0.7531, 0.7822, 0.2231, 0.0388, 0.144, 0.1134, 0)
33	(0.1076, 0.3212, 0.3644, 0.3211, 0.6773, 0.6392, 0.4342, 0.559, 0.712, 0.9352, 0.8841, 0.4095, 0.4257, 0.131, 0.0774, 1.9754, 0)
35	(0.6983, 0.796, 0.3625, 0.3012, 0.2514, 0.1598, 0.3449, 0.5826, 0.5269, 0.2746, 0.3443, 0.6698, 0.5971, 0.6582, 0.4339, 0.4226, 0.1203, 0)
37	(0.0242, 0.1193, 0.1903, 0.3682, 0.57, 0.9328, 0.7434, 0.4211, 0.5309, 0.5416, 0.6052, 0.5277, 0.7331, 0.4429, 0.4777, 0.4172, 0.043, 0.0152, 0)
39	(0.1473, 0.2929, 0.1416, 0.5286, 0.4652, 0.4965, 0.6626, 0.6447, 0.3384, 0.5618, 0.8585, 0.9491, 0.803, 0.5649, 0.3634, 0.2886, 0.07, 1.9827, 0.0663, 0)
41	(0.0664, 0.0495, 0.1414, 0.1955, 0.7154, 0.6562, 0.5504, 0.7447, 0.6492, 0.5413, 0.383, 0.4808, 0.6518, 0.7745, 0.5615, 0.5837, 0.2593, 0.1611, 0.2231, 0.1936, 0)
43	(0.6363, 0.5398, 0.5615, 0.2827, 0.4953, 0.3144, 0.2971, 0.3573, 0.1462, 0.1637, 0.6029, 0.6108, 0.5325, 0.5156, 0.6891, 0.7832, 0.6697, 0.5245, 0.2502, 1.9499, 1.9932, 0)
45	(0.1645, 0.1328, 0.2964, 0.1451, 0.1981, 0.5419, 0.8303, 0.5633, 0.7738, 0.7455, 0.7538, 0.7288, 0.4698, 0.3898, 0.2241, 0.377, 0.6715, 0.5291, 0.4697, 0.3362, 0.2116, 0.0668, 0)

TABLE IV. Phases (in units of π) of antisymmetric sequences with excitation threshold $\epsilon = 10\%$. The sequences are antisymmetric, i.e., of the form $(\phi_1, \phi_2, \dots, \phi_l, \phi_{l+1} = 0, -\phi_l, \dots, -\phi_2, -\phi_1)$ with $N = 2l + 1$. We list only the first $l + 1$ phases.

Pulse count N	Phases $(\phi_1, \phi_2, \dots, \phi_{l+1})$
3	(0.4796, 0)
5	(0.3645, 0.5224, 0)
7	(0.2602, 0.637, 0.3768, 0)
9	(0.2679, 0.4796, 0.6912, 0.2117, 0)
11	(0.7827, 0.6637, 0.122, 0.1889, 0.2195, 0)
13	(0.2954, 0.2967, 0.5593, 0.7861, 0.3226, 0.1965, 0)
15	(0.628, 0.5938, 0.6786, 0.4522, 1.9083, 0.0394, 1.9837, 0)
17	(0.4499, 0.4718, 0.2591, 0.2138, 0.4729, 0.7195, 0.346, 0.3069, 0)
19	(0.1604, 0.4132, 0.3959, 0.5442, 0.5017, 0.7561, 0.5058, 0.0744, 0.0879, 0)
21	(0.5854, 0.3046, 0.3457, 0.3471, 0.2463, 0.3761, 0.6804, 0.5324, 0.4586, 0.0287, 0)
23	(0.2819, 0.4323, 0.0969, 0.3351, 0.6166, 0.7596, 0.5734, 0.5078, 0.3885, 0.1808, 1.9856, 0)
25	(0.6081, 0.5888, 0.6566, 0.6908, 0.7123, 0.2779, 0.3276, 0.101, 1.789, 1.9087, 0.0773, 0.1536, 0)
27	(0.692, 0.6112, 0.6716, 0.6961, 0.543, 0.1473, 0.3933, 0.311, 0.18, 0.0325, 1.7255, 1.744, 1.8897, 0)
29	(1.6432, 1.7059, 1.7847, 1.7039, 1.7158, 1.3101, 1.2191, 1.3519, 1.552, 1.411, 1.5643, 1.849, 1.8274, 0.0543, 0)
31	(0.1741, 0.2498, 0.3431, 0.493, 0.4895, 0.3612, 0.5769, 0.6362, 0.5895, 0.6998, 0.605, 0.1247, 0.1155, 0.0053, 0.1562, 0)
33	(0.1435, 0.3053, 0.3383, 0.3026, 0.5877, 0.5517, 0.3699, 0.4966, 0.6328, 0.769, 0.7248, 0.3135, 0.3248, 0.0975, 0.058, 1.9817, 0)
35	(0.5883, 0.6616, 0.3128, 0.2751, 0.2333, 0.1405, 0.3266, 0.5326, 0.4848, 0.3006, 0.3435, 0.605, 0.515, 0.5453, 0.3476, 0.327, 0.0902, 0)
37	(0.08, 0.1512, 0.2045, 0.34, 0.5001, 0.8097, 0.6884, 0.4069, 0.4672, 0.4862, 0.5233, 0.4322, 0.6044, 0.3549, 0.3785, 0.3252, 0.0322, 0.0114, 0)
39	(0.1729, 0.2825, 0.1659, 0.4838, 0.3964, 0.4472, 0.586, 0.5307, 0.3071, 0.5287, 0.7521, 0.7887, 0.6426, 0.4375, 0.277, 0.2196, 0.0532, 1.9868, 0.0495, 0)

TABLE IV. (*Continued.*)

Pulse count N	Phases $(\phi_1, \phi_2, \dots, \phi_{l+1})$
41	(0.1116, 0.099, 0.1677, 0.2077, 0.6355, 0.589, 0.5094, 0.688, 0.592, 0.4895, 0.3402, 0.4179, 0.5383, 0.6326, 0.4567, 0.4611, 0.1986, 0.1243, 0.1711, 0.1463, 0)
43	(0.5417, 0.4694, 0.486, 0.2708, 0.4489, 0.2784, 0.2983, 0.3323, 0.1512, 0.2125, 0.5571, 0.5221, 0.4528, 0.4592, 0.6113, 0.6728, 0.5575, 0.4188, 0.1941, 1.9626, 1.9949, 0)
45	(0.1852, 0.1616, 0.2847, 0.1668, 0.2139, 0.4869, 0.7253, 0.4896, 0.6735, 0.6646, 0.6744, 0.6353, 0.41, 0.3337, 0.2068, 0.3288, 0.5464, 0.4222, 0.365, 0.2562, 0.1592, 0.0499, 0)

TABLE V. Phases (in units of π) of IH-optimized sequences. The sequences are antisymmetric, i.e., of the form $(\phi_1, \phi_2, \dots, \phi_l, \phi_{l+1} = 0, -\phi_l, \dots, -\phi_2, -\phi_1)$ with $N = 2l + 1$. We list only the first $l + 1$ phases.

Pulse count N	Phases $(\phi_1, \phi_2, \dots, \phi_{l+1})$
3	(0.5961, 0)
5	(0.9107, 0.2493, 0)
7	(0.8947, 0.5874, 1.8962, 0)
9	(0.8439, 1.3539, 1.8271, 1.5887, 0)
11	(1.4433, 0.7439, 0.6835, 0.3272, 0.2091, 0)
13	(1.576, 0.8705, 0.8232, 0.456, 0.3701, 0.1432, 0)
15	(1.8023, 1.0941, 1.0447, 0.6594, 0.5732, 0.3151, 0.1843, 0)
17	(0.2352, 0.8624, 1.0553, 1.2164, 1.4625, 1.6732, 1.5441, 0.0311, 0)
19	(1.8479, 1.2751, 0.981, 0.9493, 0.6312, 0.4917, 0.3592, 0.4262, 1.887, 0)
21	(1.7514, 1.3271, 1.0313, 0.8945, 0.5592, 0.5767, 0.6626, 0.4913, 1.8487, 0.0381, 0)
23	(1.6864, 1.4253, 1.1396, 0.767, 0.4155, 0.7338, 0.8962, 0.5376, 0.1081, 0.2852, 1.9109, 0)
25	(1.6293, 1.6013, 1.2881, 0.7557, 0.7333, 0.6666, 0.6003, 0.991, 0.4791, 0.1233, 0.0644, 0.1627, 0)
27	(0.2779, 1.7844, 1.3326, 1.4903, 1.1737, 0.941, 0.8286, 0.9406, 0.4875, 0.4249, 0.5421, 0.1645, 0.1325, 0)
29	(0.9509, 0.678, 0.1595, 1.9907, 0.0682, 0.031, 1.4253, 1.5511, 1.4331, 1.239, 1.1535, 0.738, 0.5688, 0.433, 0)
31	(1.0001, 1.4601, 1.756, 0.0908, 0.0722, 0.1049, 0.4856, 0.7993, 0.7721, 0.5517, 1.137, 1.2393, 1.4059, 1.6235, 1.698, 0)

[1] S. W. Hell and J. Wichmann, Opt. Lett. **19**, 780 (1994).
[2] H. Blom and J. Widengren, Chem. Rev. **117**, 7377 (2017).
[3] K. D. Stokes, C. Schnurr, J. R. Gardner, M. Marable, G. R. Welch, and J. E. Thomas, Phys. Rev. Lett. **67**, 1997 (1991).
[4] D. D. Yavuz and N. A. Proite, Phys. Rev. A **76**, 041802(R) (2007).
[5] H. Li, V. A. Sautenkov, M. M. Kash, A. V. Sokolov, G. R. Welch, Y. V. Rostovtsev, M. S. Zubairy, and M. O. Scully, Phys. Rev. A **78**, 013803 (2008).
[6] J. L. Rubio, D. Viscor, V. Ahufinger, and J. Mompart, Opt. Express **21**, 22139 (2013).
[7] A. P. Chu, K. K. Berggren, K. S. Johnson, and M. G. Prentiss, Quantum Semiclass. Opt. **8**, 521 (1996).
[8] R. Abfalterer, C. Keller, S. Bernet, M. K. Oberthaler, J. Schmiedmayer, and A. Zeilinger, Phys. Rev. A **56**, R4365(R) (1997).
[9] K. S. Johnson, J. H. Thywissen, N. H. Dekker, K. K. Berggren, A. P. Chu, R. Younkin, and M. Prentiss, Science **280**, 1583 (1998).
[10] J. H. Thywissen and M. Prentiss, New J. Phys. **7**, 47 (2005).
[11] J. Mompart, V. Ahufinger, and G. Birkl, Phys. Rev. A **79**, 053638 (2009).
[12] A. V. Gorshkov, L. Jiang, M. Greiner, P. Zoller, and M. D. Lukin, Phys. Rev. Lett. **100**, 093005 (2008).
[13] C. Weitenberg, M. Endres, J. F. Sherson, M. Cheneau, P. Schauß, T. Fukuhara, I. Bloch, and S. Kuhr, Nature (London) **471**, 319 (2011).
[14] D. Viscor, J. L. Rubio, G. Birkl, J. Mompart, and V. Ahufinger, Phys. Rev. A **86**, 063409 (2012).
[15] S. S. Ivanov and N. V. Vitanov, Opt. Lett. **36**, 1275 (2011).
[16] N. V. Vitanov, Phys. Rev. A **84**, 065404 (2011).
[17] J. T. Merrill, S. C. Doret, G. Vittorini, J. P. Addison, and K. R. Brown, Phys. Rev. A **90**, 040301(R) (2014).
[18] T. Zhong and P. Goldner, Nanophotonics **8**, 2003 (2019).
[19] J. G. Bartholomew and M. J. Sellars, J. Lumin. **194**, 284 (2018).
[20] R. Kolesov, S. Lasse, C. Rothfuchs, A. D. Wieck, K. Xia, T. Kornher, and J. Wrachtrup, Phys. Rev. Lett. **120**, 033903 (2018).
[21] S.-Y. Lan, A. G. Radnaev, O. A. Collins, D. N. Matsukevich, T. A. B. Kennedy, and A. Kuzmich, Opt. Express **17**, 13639 (2009).
[22] M. Stabel, L. D. Feldmann, and T. Halfmann, J. Phys. B: At., Mol. Opt. Phys. **55**, 154003 (2022).
[23] G. Corrielli, A. Seri, M. Mazzera, R. Osellame, and H. de Riedmatten, Phys. Rev. Appl. **5**, 054013 (2016).
[24] H. R. Hamedi, G. Žlabys, V. Ahufinger, T. Halfmann, J. Mompart, and G. Juzeliūnas, Opt. Express **30**, 13915 (2022).
[25] J. Evers, S. Qamar, and M. S. Zubairy, Phys. Rev. A **75**, 053809 (2007).
[26] S. Subhankar, Y. Wang, T.-C. Tsui, S. L. Rolston, and J. V. Porto, Phys. Rev. X **9**, 021002 (2019).
[27] M. McDonald, J. Trisnadi, K.-X. Yao, and C. Chin, Phys. Rev. X **9**, 021001 (2019).

[28] Z.-H. Qian, J.-M. Cui, X.-W. Luo, Y.-X. Zheng, Y.-F. Huang, M.-Z. Ai, R. He, C.-F. Li, and G.-C. Guo, Phys. Rev. Lett. **127**, 263603 (2021).
[29] K. T. Kapale, in *Progress in Optics 58*, 1st ed., edited by E. Wolf (Elsevier, Amsterdam, 2013), pp. 199–250.
[30] M. H. Levitt, Prog. Nucl. Magn. Reson. Spectrosc. **18**, 61 (1986).
[31] M. H. Levitt, in *eMagRes*, edited by R. K. Harris and R. L. Wasylishen (Wiley, Hoboken, NJ, 2007).
[32] J. T. Merrill and K. R. Brown, in *Quantum Information and Computation for Chemistry*, Advances in Chemical Physics No. 154, edited by S. A. Rice, A. R. Dinner, and S. Kais (Wiley, Hoboken, New Jersey, 2014), pp. 241–294.
[33] T. Peters, S. S. Ivanov, D. Englisch, A. A. Rangelov, N. V. Vitanov, and T. Halfmann, Appl. Opt. **51**, 7466 (2012).
[34] E. S. Dimova, S. S. Ivanov, G. S. Popkirov, and N. V. Vitanov, J. Opt. Soc. Am. A **31**, 952 (2014).
[35] G. Wolfowicz and J. J. Morton, in *eMagRes*, edited by R. K. Harris and R. L. Wasylishen (Wiley, Chichester, 2016), pp. 1515–1528.
[36] A. M. Souza, G. A. Álvarez, and D. Suter, Philos. Trans. R. Soc. A **370**, 4748 (2012).
[37] C. P. Koch, U. Boscain, T. Calarco, G. Dirr, S. Filipp, S. J. Glaser, R. Kosloff, S. Montangero, T. Schulte-Herbrüggen, D. Sugny, and F. K. Wilhelm, EPJ Quantum Technol. **9**, 19 (2022).
[38] M. James, Annu. Rev. Control, Robotics, Auton. Syst. **4**, 343 (2021).
[39] S. Wimperis, J. Magn. Reson., Ser. A **109**, 221 (1994).
[40] K. R. Brown, A. W. Harrow, and I. L. Chuang, Phys. Rev. A **70**, 052318 (2004).
[41] G. T. Genov, B. T. Torosov, and N. V. Vitanov, Phys. Rev. A **84**, 063413 (2011).
[42] B. T. Torosov and N. V. Vitanov, Phys. Rev. Res. **2**, 043194 (2020).
[43] C. Zhang, L.-T. Shen, J. Song, Y. Xia, and Z.-C. Shi, Opt. Express **32**, 1188 (2024).
[44] B. T. Torosov, S. S. Ivanov, and N. V. Vitanov, Phys. Rev. A **102**, 013105 (2020).
[45] B. T. Torosov and N. V. Vitanov, Phys. Rev. A **107**, 032618 (2023).
[46] B. T. Torosov, E. S. Kyoseva, and N. V. Vitanov, Phys. Rev. A **92**, 033406 (2015).
[47] A. Shaka and R. Freeman, J. Magn. Reson. **59**, 169 (1984).
[48] R. Tycko and A. Pines, Chem. Phys. Lett. **111**, 462 (1984).
[49] R. Tycko, A. Pines, and J. Guckenheimer, J. Chem. Phys. **83**, 2775 (1985).
[50] A. Shaka, J. Keeler, M. Smith, and R. Freeman, J. Magn. Reson. (1969) **61**, 175 (1985).
[51] B. T. Torosov and N. V. Vitanov, Phys. Rev. A **99**, 013424 (2019).
[52] E. Kyoseva, H. Greener, and H. Suchowski, Phys. Rev. A **100**, 032333 (2019).
[53] S. S. Ivanov, B. T. Torosov, and N. V. Vitanov, Phys. Rev. Lett. **129**, 240505 (2022).
[54] G. H. Zhang, B. Braverman, A. Kawasaki, and V. Vuletić, Rev. Sci. Instrum. **86**, 126105 (2015).
[55] M. Nilsson, L. Rippe, S. Kröll, R. Klieber, and D. Suter, Phys. Rev. B **70**, 214116 (2004).
[56] F. Beil, J. Klein, G. Nikoghosyan, and T. Halfmann, J. Phys. B: At., Mol. Opt. Phys. **41**, 074001 (2008).
[57] N. Rosen and C. Zener, Phys. Rev. **40**, 502 (1932).
[58] Y. N. Demkov, J. Exptl. Theoret. Phys. **45**, 195 (1963) [Sov. Phys. JETP **18**, 138 (1964)].
[59] L. S. Simeonov and N. V. Vitanov, Phys. Rev. A **89**, 043411 (2014).
[60] B. T. Torosov and N. V. Vitanov, J. Phys. A: Math. Theor. **41**, 155309 (2008).